ICAS 2016
30th Congress of the International Council of the Aeronautical Sciences
DCC, Daejeon, Korea ; September 25-30, 2016

ACTIVE VORTEX FLOW CONTROL ON A GENERIC DELTA WING

Andrei Buzica*, Julius Bartasevicius*, Christian Breitsamter*
***Chair of Aerodynamics and Fluid Mechanics, Technical University of Munich**

Keywords: *Aerodynamics, Flow Control, PIV, High Angle of Attack*

Abstract

The flow around delta wings is dominated by a leading-edge vortex system, which induces increased velocities above the wing hence producing high suction peaks. These are responsible for the lift needed at high angle of attack aircraft maneuvering. In the flight regime beyond stall the flow separating from the leading-edge encounters a very steep adverse pressure gradient and consequently doesn't roll up into a vortex-like structure. Rather, encloses a massive dead-water region over the entire wing. With unsteady jet blowing at the leading edge additional momentum is created that reattaches the flow at the wing surface thus increasing the lift significantly. The investigated flow control method can be applied for extending the flight envelope, increasing maneuvering capability and flight stability.

This flow manipulation technique is investigated on a generic half wing model at a very high angle of attack (α = 45°) in a low speed wind tunnel using force measurements and stereoscopic particle image velocimetry. Assessment of different actuation strategies is comprised in this study, in which blowing frequency and relative phase shift of the blowing momentum are kept constant and also modulated along the leading-edge.

Nomenclature

C_L	lift coefficient [-]
c_r	root chord [m]
C_μ, $C_{\mu,i}$	net and individual blowing momentum coefficient [-]
Δd	grid spacing in the PIV plane [mm]
DC	duty cycle [%]
f, f_{dom}	frequency and dominant frequency [Hz]
F^+	dimensionless frequency $F^+ = f \cdot c_r / U_\infty$ [-]
l_μ	mean aerodynamic chord $l_\mu = 2/3 c_r$ [m]
Ma	Mach number [-]
$Re_{l\mu}$	Reynolds number based on the mean aerodynamic chord [-]
t	time [s]
T	blowing period T = 1/f [s]
TKE	turbulent kinetic energy [m^2/s^2]
Tu	turbulence level [%]
u, v	wing-fixed axial and lateral velocity components [m/s]
u_{min}	minimum axial velocity components [m/s]
U_∞	freestream velocity [m/s]
U_j	jet velocity [m/s]
x, y, z	wing fixed coordinates [m]
α	angle of attack [°]
δ	wing thickness [m]
Γ_x	axial circulation [m^2/s]
φ	leading-edge sweep [°]
Λ	aspect ratio [-]
θ	phase angle [°]
ω_x	axial vorticity [1/s]
2D3C	two dimensional, three component
F12	dynamic blowing at f = 12 Hz
FV1, FV2	frequency variation 1 and 2
Nd:YAG	neodymium-doped yttrium aluminum garnet
PV1-4	phase variation 1-4
sCMOS	scalable complementary metal-oxide semiconductor

1 Introduction

1.1 Delta Wing Aerodynamics

Aircraft configurations with delta shaped wings have been successfully developed and operated for decades in both military and civil applications. These wings are characterized by a low aspect ratio, high sweep angle of the leading-edge (LE) and low wing thickness. The flow around delta wings at high angles of attack (AoA's) consists of two counter rotating large vortices above the wing, which accelerate the fluid near the wall generating high suction peaks. Delta wings can thus achieve additional non-linear lift compared to conventional configurations, making them superior in maneuverability, stability and control [1].

The large vortex originating from the rollup of the separated shear-layer has different evolution stages depending on the sweep and AoA of the delta wing (Fig. 1):

1. At low AoA's a weak vortex is formed close to the wing tip, which develops in direction of the apex as the incidence is increases.
2. The vortex is fully developed along the whole LE and it moves inboards and upwards with increasing incidence. At the same time the vortex strength increases as well.
3. Above a certain AoA the vortex on the suction side of highly swept wings gets fixed in span-wise direction. The vortex pair share the same reattachment line.
4. Vortex breakdown occurs by reaching a critical flow state [2]. It causes a sudden expansion of the vortex cross section, axial deceleration in the core and pressure increase downstream. These have a detrimental effect on the aerodynamic performances. The breakdown location shifts towards the apex if the AoA is further increased.
5. At stall the breakdown location reaches the apex. Beyond the maximum AoA the pressure gradient around the LE is so high, that the flow fails to reattach on the wing's surface forming a dead-water region on the upper side.

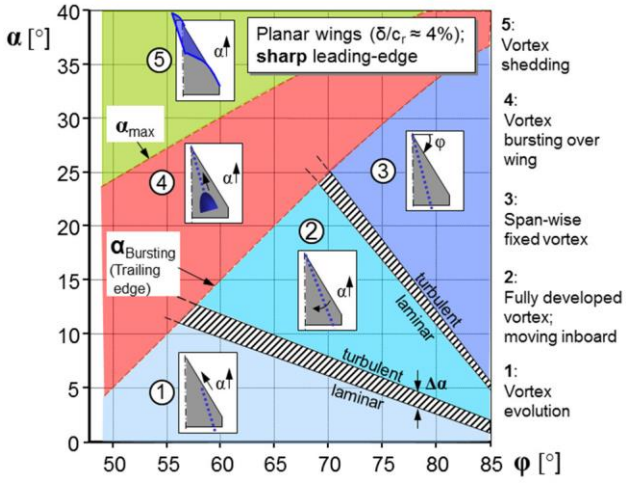

Fig. 1. Leading-edge vortex evolution for delta wings [3]

The vortical flow field around delta wings has an unsteady nature during all flight regimes. Instabilities occur over a broad frequency spectrum [1], [4]. Discrete vortices are shed from the LE with a typical frequency [5]. They pair up and transport in a spiral manner the circulation into the large LE vortex [6]. When breakdown occurs over the wing, the almost conical flow changes its structure downstream, and becomes highly unsteady. Downstream of the breakdown location, which oscillates with a low frequency, the vortex core forms a spiral and dissipates into turbulence after a few twists. This phenomenon is called Helical-mode-instability, because the original core flow forms a helix and measures fluctuations within a narrow frequency range. Fig. 2 displays the spectrum of typical unsteady flow phenomena for delta wings.

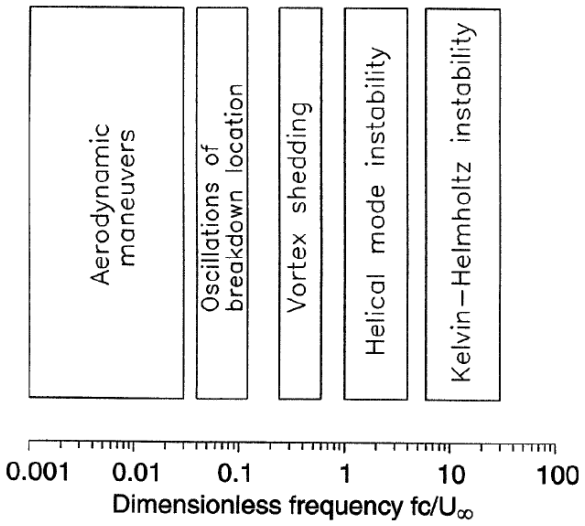

Fig. 2. Spectrum of unsteady flow phenomena over delta wings as function of dimensionless frequency [7]

1.2 Flow Control for Delta Wings

A great potential of increasing the aerodynamic performance of wing configurations with LE vortex systems lies in manipulating the flow by active and passive control mechanisms. The latter ones can influence the flow through generating additional stabilizing vortices, i.e. from canard-wing or double-delta wing configurations, and through unsteady excitation by flow induced motions of a flexible wing [8]. Passive flow control has the disadvantage, that its effectiveness is designed for only a few flight conditions, i.e. strakes being effective at high AoA's maneuvers but unnecessary during cruise.

For that reason active flow control is more appealing in the aircraft design. Many mechanisms for actively controlling the flow around delta wings have been investigated [8], [9]. They include various suction and blowing setups [10-13], adaptive or oscillating flaps and plasma actuators. It has been demonstrated, that unsteady control mechanisms are more effective than steady ones. The reason is that the unsteady phenomena shown in Fig. 2 can be targeted by flow excitation within the dominant frequency range in the region where the phenomenon occurs. Flow control mechanisms for delta wings and control of vortex breakdown are outlined in [8] and [9] respectively. In the following the effects of pulsed blowing/suction at the LE of delta wings will be briefly presented.

Unsteady leading edge blowing and suction with a subharmonic of the natural vortex shedding frequency has successfully changed the flow structure and ordered the vortex pairing [11]. Other studies had shown, that vortex breakdown can be delayed by the same actuation mechanism when the non-dimensional actuation frequency is in the range of the helical-mode-instability $F^+ = O(1)$ [10], [12], [14].

In the current study the effect of pulsed LE blowing is analyzed experimentally on a sweptback ($\varphi = 65°$) generic half delta wing at a post-stall angle of $\alpha = 45°$. At this extreme flight conditions the separating shear layer doesn't roll up into a vortical structure, hence only vortex shedding is present in the flow. With active excitation previous measurements proved the reformation of a vortex like structure above the wing [3]. A more detailed investigation on the flow field comprised in this study should complete the experimental database. Therefore, additional stereoscopic particle image velocimetry (PIV) planes had been analyzed in order to reconstruct the average three dimensional flow field for different actuation modes. Force measurements confirm the flow field data. In addition, phase-averaged PIV at certain cross-flow planes help to understand the interaction between the induced disturbances and the outer flow.

2 Experimental Setup

2.1 Wind Tunnel Facilities

The experiments were conducted in the closed loop, low speed wind tunnel facilities at the Chair of Aerodynamics and Fluid Mechanics of the Technical University of Munich. PIV and force measurements were conducted in the wind tunnel A (WTA), which is operated with an open test section. Its inlet has a 1.8 m × 2.4 m cross section and the collector is 4.8 m farther downstream. The measurements have been conducted at a freestream velocity of $U_\infty = 12$ m/s ($Re_\mu = 5 \cdot 10^5$, Ma = 0.036) with a deviation of $\Delta U_\infty \leq 0.15$ m/s and an inlet turbulence level of Tu < 0.4%.

2.2 Wind Tunnel Model

The wind tunnel model has the geometry of the VFE-2 configuration ($\varphi = 65°$, $\Lambda = 1.87$) on which extensive experimental data has been obtained for CFD validation purposes [15], [16], [17]. The half wing measuring 0.977 m at the root chord is manufactured by two metal plates connected by the sharp contoured leading and trailing edge, made from reinforced plastic [14]. The model (see Fig. 3) is equipped with a 0.055 m wide péniche that elevates the wind tunnel model from the test

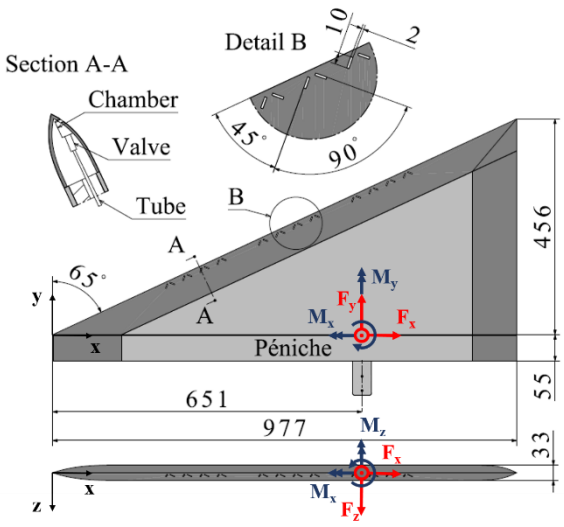

Fig. 3. Sketch of the wind tunnel model with LE blowing system and representation of force and moment coordinate system.

section's boundary layer. The relative wing thickness of δ/c_r = 3.38% allows the housing of the pneumatic actuation system. Pressurized air is distributed by a tubing system to twelve pressure chambers positioned inside the LE. Each chamber has a two point operating valve (open and closed) at its inlet. Due to pressure difference, while the valves are open, the air evacuates the chambers through slot pairs and is injected into the outer flow normal to the wing's upper surface. The slots have a high aspect ratio (2 mm × 10 mm). The slots are arranged pair-wise, they form a right angle to each other and are angled at 45° with respect to the LE. This slot geometry is favorable for the creation of discrete vortices, which are fed into the separated shear layer forming at the LE.

By adjusting the inlet pressure to the actuating system and the time the valves are open or closed an actuation step signal is produced. Parametric variation comprising of frequency, duty cycle and phase displacement can be achieved for each slot individually. Furthermore the blowing can be operated by varying the frequency and phase along the LE.

2.3 Measurement Technique

In WTA the model is mounted on a six-component external balance positioned under the test section floor. In the whole measurement range the absolute error of the lift coefficient lies within $C_{L,err} \leq \pm 0.025$. AoA adjustment is enabled through rotation of the balance and the floor plate, on which the péniche is connected. However, the AoA for the current setup is fixed at α = 45°. In order to measure the aerodynamic forces that are acting on the half wing, contact to the péniche has been eliminated. The moment reference point lies in the wing's symmetry plane and at 2/3 of the root chord downstream of the apex. The forces are defined in the body fixed system, see Fig. 3.

The experimental setup in WTA is presented in Fig. 4. The PIV components are mounted on a traverse system located above the test section. The light source is a 325 mJ Nd:YAG double cavity laser producing a wavelength of 532 nm. By going through a widening optic it forms a 5µm thin light sheet illuminating the measurement plane. The flow field velocities are measured in cross-flow planes normal to the wing as well as along the axis of the vortical structure by applying the 2D3C, double frame and single exposure technique. While for the cross-flow planes the cameras were mounted above the test section, as in Fig. 4, the measurements along the vortex core were conducted with the cameras mounted sideways. For each measurement per plane and parametric variation 400 samples are recorded at a frequency of 13 Hz by two sCMOS cameras with lenses and Scheimpflug adapters. According to [18] the maximum velocity uncertainty is estimated at $|u_{err}/U_\infty| = |v_{err}/U_\infty| \leq 0.02$. A programmable timing unit (PTU) synchronizes the cameras with the laser. For phase-averaged recordings, the PTU was triggered externally by the rising edge of the valve control signal. For this measurements the recording frequency is matched to a division of the actuation frequency, which was set at f = 12 Hz.

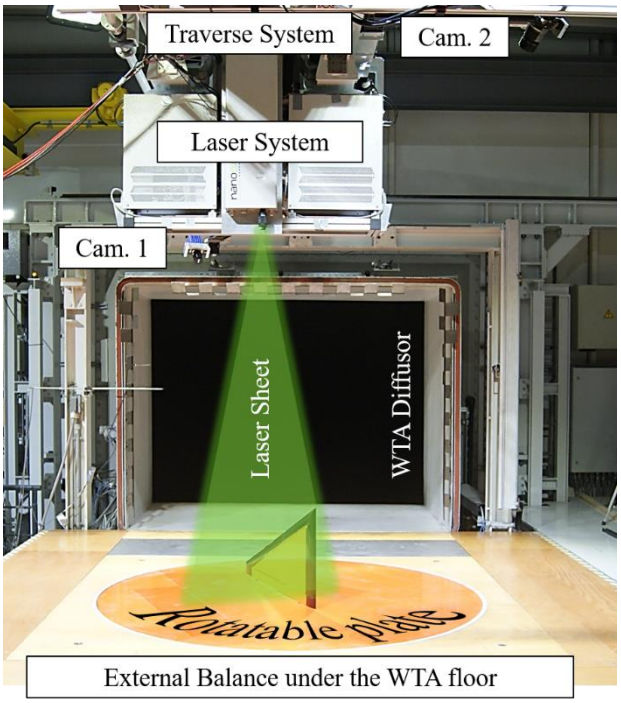

Fig. 4. Setup of the half wing model and the PIV system in WTA test section for cross-flow planes measurement.

The resolution of the measured velocity field depends on the camera lenses (50/130 mm focal length) and the camera position relative to the measurement plane. Cross-flow planes at locations $x/c_r \leq 55\%$ have a grid spacing of Δd = 3.4 – 3.7 mm whereas for the aft planes Δd = 8.9 mm resulted. Because the bigger flow structure at the rear half of the wing had to be recorded, the lenses with the focal length of 50 mm were used at those locations.

Based on previous measurements [3], the vortex axis of the excited flow field (f = 12 Hz) was determined at discrete chord-wise positions. The measurement plane through the vortex is spanned by the vortex axis and a line parallel to the wing's y-axis. This plane creates an angle of 11° with the wing and is 10 mm distant from the wing's apex.

3 Actuation Strategies

In the current study different actuation strategies are investigated and compared, in which the frequency and phase displacement of the pulsed blowing are both constant and modulated along the leading edge. The blowing momentum coefficient and duty cycle are set for each slot pair at $C_{\mu i} = 2.63 \cdot 10^{-3}$ and DC = 25% respectively. This results in a net blowing momentum of $C_{\mu} = 12 \cdot C_{\mu i} = 3.16 \cdot 10^{-2}$.

In the constant frequency case all 12 slots are operated at a blowing frequency of f = 12 Hz (F^+ = 1). The investigated frequency variations are plotted as a function of the chord-wise slot position x/c_r in Fig. 5: F12 stands for the case whit constant frequency; FV1 and FV2 are two cases with decreasing frequency along the LE. The frequency variation 1 (FV1) has a constant frequency for each segment (4 slot pairs) and a frequency downstream decrease between segments. The dimensionless frequencies per segment are set at F+ = 0.7, 1.0, 1.3 in stream-wise order.

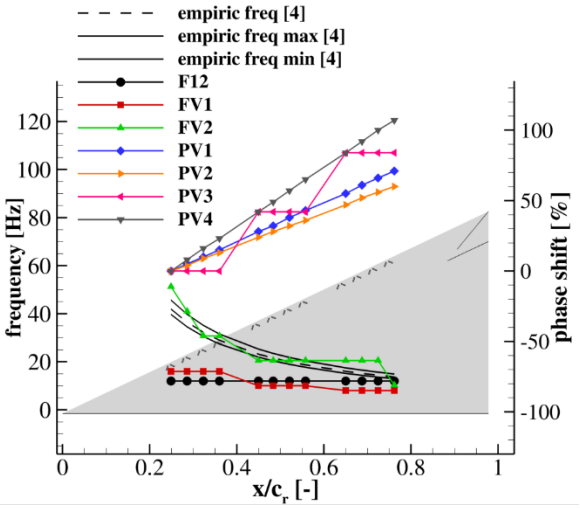

Fig. 5. Frequency (F12, FV1 and FV2) and relative phase shift variations (PV1, PV2, PV3 and PV4) of the blowing momentum versus the slot-pair position.

Based on extensive hot-wire measurements on delta wings [4] the natural dominant frequency of the typical burst vortex structure at high angles of attack can be predicted with the following empiric formula:

$$f_{dom} = \frac{1}{x \cot \varphi \sin \alpha} \frac{U_\infty}{} (0.28 \pm 0.025)\ [4] \qquad (1)$$

For the present geometry at freestream conditions of $\alpha = 45°$ and $U_\infty = 12$ m/s the dominant frequency is distributed as shown in Fig. 5 by the dotted line. Because the turbulent scales are growing stream-wise, i.e. the burst structure expands, the natural frequency decreases inverse proportional to the local chord. By actuating with a spatially decreasing frequency as in the frequency variation 2 (FV2) a reconstruction of a vortex-like structure is expected. During actuations with spatial frequency variation the phase displacement for each slot has been set to zero.

Considering the downstream disturbance propagation variations of phase displacement are additionally tested. For this purpose four strategies are investigated (see Fig. 5). The actuation frequency is constant at f = 12 Hz. Relative to the first slot pair the phase is increased linearly in chord direction for PV1, PV2 and PV4 and stepwise for PV3.

4 Results and Discussion

4.1 Aerodynamic loads

The lift-coefficient polar of the baseline is plotted in Fig. 6 in the range $0° \leq \alpha \leq 50°$. The freestream conditions are set by the Reynolds number at $Re_{l\mu} = 5 \cdot 10^5$ and the Mach number at Ma = 0.036. The C_L-α slope is typical for the sharp-edged planar delta wings. The discontinuity at $\alpha \approx 20°$ indicates, that vortex breakdown occurs for the first time over the wing. The maximum lift coefficient is reached at an angle of attack of $\alpha \approx 35°$. In the post-stall flight regime a sharp drop in lift of 35.5% is present at $41° \leq \alpha \leq 42°$. This is caused by a massive flow separation on the wing's upper side. With dynamic blowing this sudden lift decrease in the post-stall regime is eliminated. The first diagram of Fig. 6 includes the results of the lift coefficient for the different frequency variations (FV1 and FV2) while the second diagram the lift coefficients for the phase variations (PV1-4). In both plots the lift coefficients of the cases with variable parameters (FV and PV) are compared to those of the baseline and the actuation with constant frequency and phase (F12). The following observations are deduced from the upper diagrams of Fig. 6:

- Dynamic blowing with both constant and modulated frequencies can increase the lift by more than 50% compared to the non-actuated case at $\alpha \geq 42°$.
- FV2 is more dependent on the angle of attack. The lift slope is therefore steeper compared to F12 and FV1. The reason is that FV2 reconstructs the dominated frequencies for one specific angle of $\alpha = 45°$.
- For all investigated AoA's FV1 produces lower lift gains than F12 although the non-dimensional frequency range for FV1 (F^+ =

0.7, 1.0, 1.3) lies around unity. A possible reason is that the energy of the blowing momentum is divided in the spectral domain and not concentrated on one frequency as in F12.

- By blowing with the same frequency through all twelve slot pairs the gradient of the relative lift-gain $\Delta C_L/C_{L,Baseline}$ as function of α is the most moderate one (see Fig. 6 and Table 1). F12 is therefore less dependent on the AoA than the other two actuation strategies, making it preferable for AFC applications.

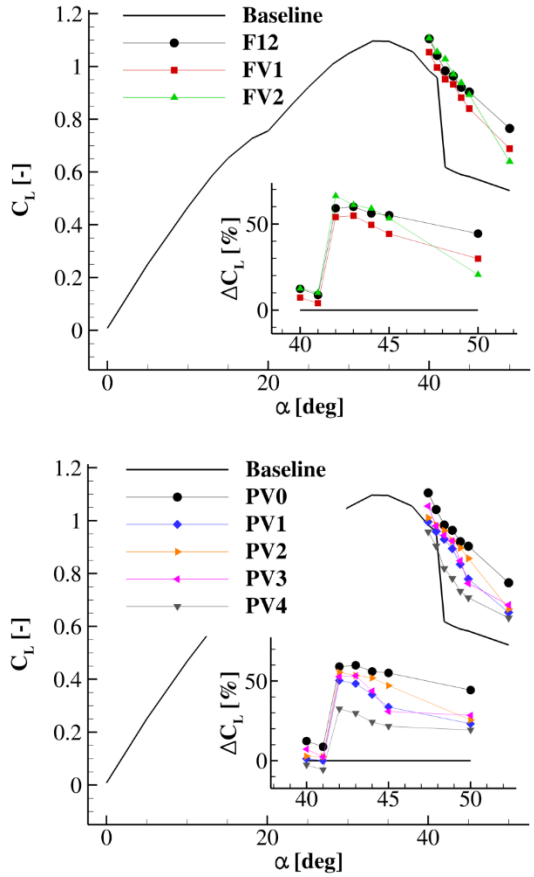

Fig. 6. Lift coefficient C_L versus AoA for the baseline and actuated case with constant and spatially modulated frequency (above) and phase (below) at $Re_{l\mu} = 5{\cdot}10^5$ and Ma = 0.036.

α		42°	45°	50°
$\frac{\Delta C_L}{C_{L,Baseline}}$ [%]	F12	59.1	55.1	44.4
	FV1	53.9	44.2	29.9
	FV2	66.3	53.3	20.7
	PV2	55.6	47.2	25.6

Table 1. Difference of lift coefficient of the four actuation strategies (F12, FV1, FV2 and PV2) relative to the lift coefficient of the baseline for three post-stall angles of attack.

According to the lower diagrams of Fig. 6 the lift characteristic in the post-stall region is negatively correlated to the downstream phase displacement between the blowing slots, i.e. the lift curve is shifted towards lower C_L values with increasing relative phase delay. In conclusion the shear layer is more receptive if the slots are synchronized. This observation is in concordance to results of force measurements on a 60° swept delta wing with LE suction/blowing at high incidences [10]. In addition to the linear phase variation along the leading edge (PV1, PV2 and PV4) a stepwise variation (PV3) is investigated. By synchronizing the slots in each segment and increasing the time lag downstream between the three segments a better lift gain is observed in comparison to the linear variation with the same slope. This attests the quasi-two-dimensional receptivity of the shear layer [10].

4.2 Average Flow Field

4.2.1 Cross-Flow PIV Planes

The flow fields obtained from PIV provides detailed information on the actuation impact stated by the force measurements discussed in the previous subchapter. The averaged three-dimensional velocity field above the wing is reconstructed by interpolating values from cross-planes measured at each 5% of the root chord. Fig. 7 presents four selected cases (Baseline, F12, FV2 and PV2), in which isosurfaces of velocity components with streamlines passing above the LE are shown.

The blue colored isosurfaces of the zero axial velocity enclose the reverse-flow region on the wing's suction side. Outside this region the axial velocity is positive. Without actuation the flow is completely separated at α = 45°, as demonstrated by the negative axial velocity region above the entire wing surface. With active unsteady blowing the separated flow topology changes to a vortex-like structure. The reverse-flow region decreases in size and furthermore a near wall region with vortex-induced high span-wise velocities is generated. Inside the yellow surfaces of Fig. 7 velocity components of $v/U_\infty \geq 0.7$ are present. The induced span-wise velocity produces suction thus increasing the lift coefficient.

The actuation strategy with spatially synchronized blowing (F12) is more effective than strategies with frequency (FV2) and phase (PV2) variation along the LE. The extra lift generated by the actuation is positively correlated to the near-wall induced velocities. Thus F12 generates a stronger

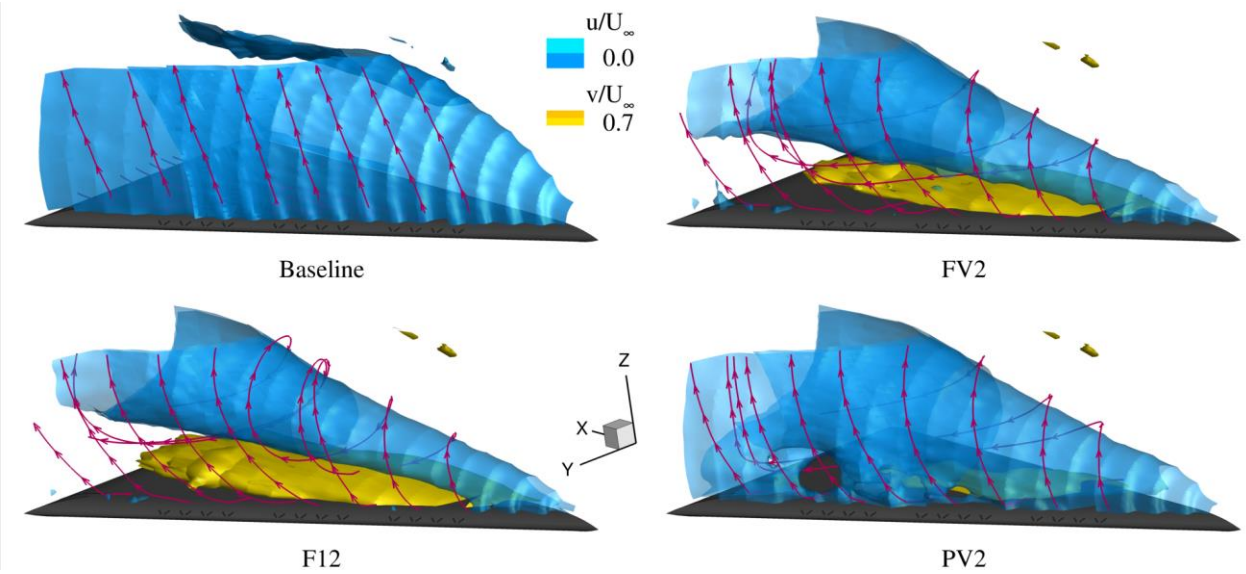

Fig. 7. Isosurfaces of non-dimensional average velocity components u/U∞ = 0.0 (blue) and v/U∞ = 0.7 (yellow) and streamlines measured by stereo PIV for the baseline, F12, FV2 and PV2 cases, at $Re_{\mu} = 5 \cdot 10^5$, Ma = 0.036 and α = 45°

vortex, which produces higher lift, see Fig. 7 and Table 1.

PV2 generates the least additional lift compared to the other two actuated cases F12 and FV2. In Fig. 7, bottom right, a rather non-uniform flow structure is observed. The blowing slots work with a certain phase delay producing zones with increased shear values downstream of the blowing segments. The flow is more heterogeneous in this case, as demonstrated by the "holes" in the isosurface $u/U_\infty = 0$. FV2 produces a similar flow structure as F12, but with a larger reverse-flow region in the vortex core and lower swirl angles. In the next chapters the synchronized blowing F12 will be further discussed.

4.2.2 Longitudinal PIV Planes

From longitudinal measurement planes positioned as described in 2.3.1 the downstream evolution of the flow close to the wing's upper surface is presented in Fig. 8. It compares both cases, the baseline and the unison blowing F12, at the same freestream conditions as in the previous chapter.

The dimensionless axial velocity is plotted in the range from $u/U_\infty = -0.25$, encountered in the case without blowing above the wing, to $u/U_\infty = 0.7$, values of the freestream flow. In the non-actuated case two regions are distinguished: outer and reverse flow over the wing. These regions are separated by the shear layer originating at the sharp LE. Moderate values of the turbulent kinetic energy, $TKE/U_\infty^2 \geq 0.05$, are present in this mixing layer. The outer flow decelerates and converges with the reversed flow above the wing into one line situated inboard of the shear layer. The fluid is transported in z-direction and upstream with no reattachment on the wing's surface.

Pulsed blowing reattaches the separated shear layer, generating a vortex-like structure with reverse flow in the core. The axial velocity span-wise distribution recreates a wake-type profile. By injecting unsteady momentum into the flow the turbulence levels rise above $TKE/U_\infty^2 = 0.15$ on the suction side. It is distributed almost homogeneously, indicating that the flow is responsive to the excitation. In the F12 case the streamlines of the far-field flow have a smaller angle to the x-axis. In conclusion, the LE pulsed blowing effects as well the upstream flow. The convergence curve of the streamlines in the actuated case bends in x-direction in the vicinity of the blowing slots. The fluid transport is influenced by the shear-layer rollup and is directed downstream to the wing's surface. Along the LE the flow accelerates above the slots at $x/c_r \approx 0.25$ (see the lower plot of Fig. 8), indicating the local effect of discretely distributed blowing slots along the LE. Heterogeneity is observed as well in the reverse flow region where a negative axial velocity peak is located downstream of the first blowing segment, at $0.33 \leq x/c_r \leq 0.49$. The negative peaks of the axial velocity are plotted chord-wise in Fig. 9 for both cases F12 and FV2. It is obvious that the segment position is correlated with the regions of increased upstream velocities.

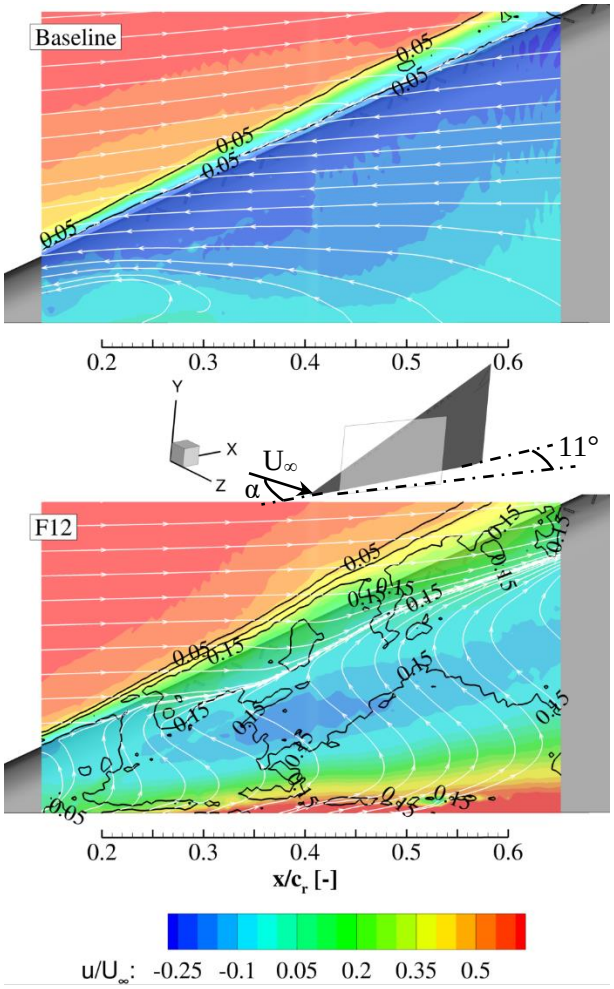

Fig. 8. Longitudinal PIV plane indicating non-dimensional axial velocity contour, turbulent kinetic energy isolines and in-plane streamlines for the baseline case (above) and the F12 case with $F^+ = 1$ (below), at $Re_{l\mu} = 5 \cdot 10^5$, Ma = 0.036 and $\alpha = 45°$.

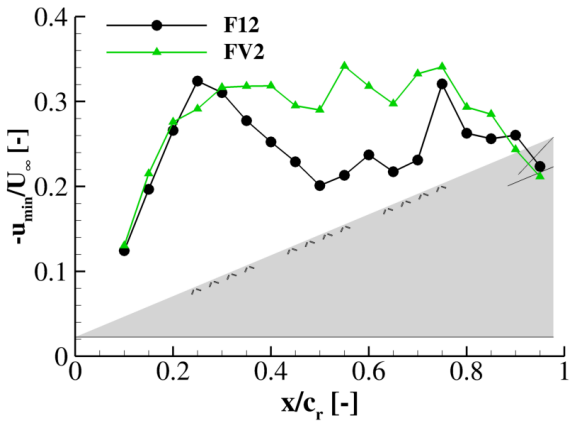

Fig. 9. Chord-wise distribution of the negative axial velocity peaks for blowing with constant (F12) and variable frequency (FV2) at $Re_{l\mu} = 5 \cdot 10^5$, Ma = 0.036 and $\alpha = 45°$.

4.3 Phase-averaged Flow Field

In this chapter the average evolution during one blowing period is analyzed by comparing eight phase-averaged frames equally distributed over the period, see Fig. 10. The phase displacement is constant at $\Delta\theta = 45°$, equivalent to a time-step size of approximately $\Delta t \approx 0.01$ s (one period lasts T = 1/f = 0.0833 s). The PIV cross-flow planes are located at x/c_r = 0.20, 0.40, 0.60, 0.65 and 0.80. The jet velocity U_j is plotted schematically as a function of the phase angle θ, see Fig. 10a. The phase angle has the value $\theta = 0°$ when the valve is opening and $\theta = 90°$ while closing. At $\theta = 45°$ the blowing jet velocity has the maximum value of $U_j \approx 65$ m/s. Because the valves are operated with a duty cycle of DC = 25%, in the range $90° < \theta < 360°$ the valves are closed and therefore the blowing momentum is zero.

The eight measured phases are presented in Fig. 10b. In each crossflow plane the phase-averaged axial vorticity ω_x related to the quotient of the freestream velocity U_∞ and the mean aerodynamic chord l_μ is plotted in the range $0.5 \leq \omega_x(l_\mu/U_\infty) \leq 3.0$. In each frame of Fig. 10b the areas with high vorticity peaks decrease in stream-wise direction. In the first plane, at $x/c_r = 0.2$, high vorticity values are concentrated in the shear layer. The flow structure in this plane is quasi stationary, indicating a low upstream influence of the dynamic blowing. Farther downstream the active blowing changes the flow structure at each measured time step. The regions with high vorticity are decreasing downstream in all eight phases. On the other hand, the positive dimensionless circulation $\Gamma_x/(U_\infty l_\mu)$ increases downstream. This variable is defined as the surface integral of the positive axial vorticity. Fig. 10c includes a surface plot of the circulation as a function of the local chord x/c_r and the phase θ. The vortices originating from the lower wing surface get fed into the shear layer that rolls up above the wing thus contributing to the downstream circulation increase. In the first plane at $x/c_r = 0.20$, the circulation is nearly constant throughout the phases. Farther downstream, at $x/c_r = 0.40$, the circulation decreases slightly during one blowing period. Close to the trailing edge the positive circulation is more dependent on the phase angle. The phase delay between the valve opening ($\theta = 0°$) and the circulation peaks is $\Delta\theta \approx 315°$ and $\Delta\theta \approx 360°$ for $x/c_r = 0.65$ and $x/c_r = 0.80$ respectively, suggesting a downstream vortex convection.

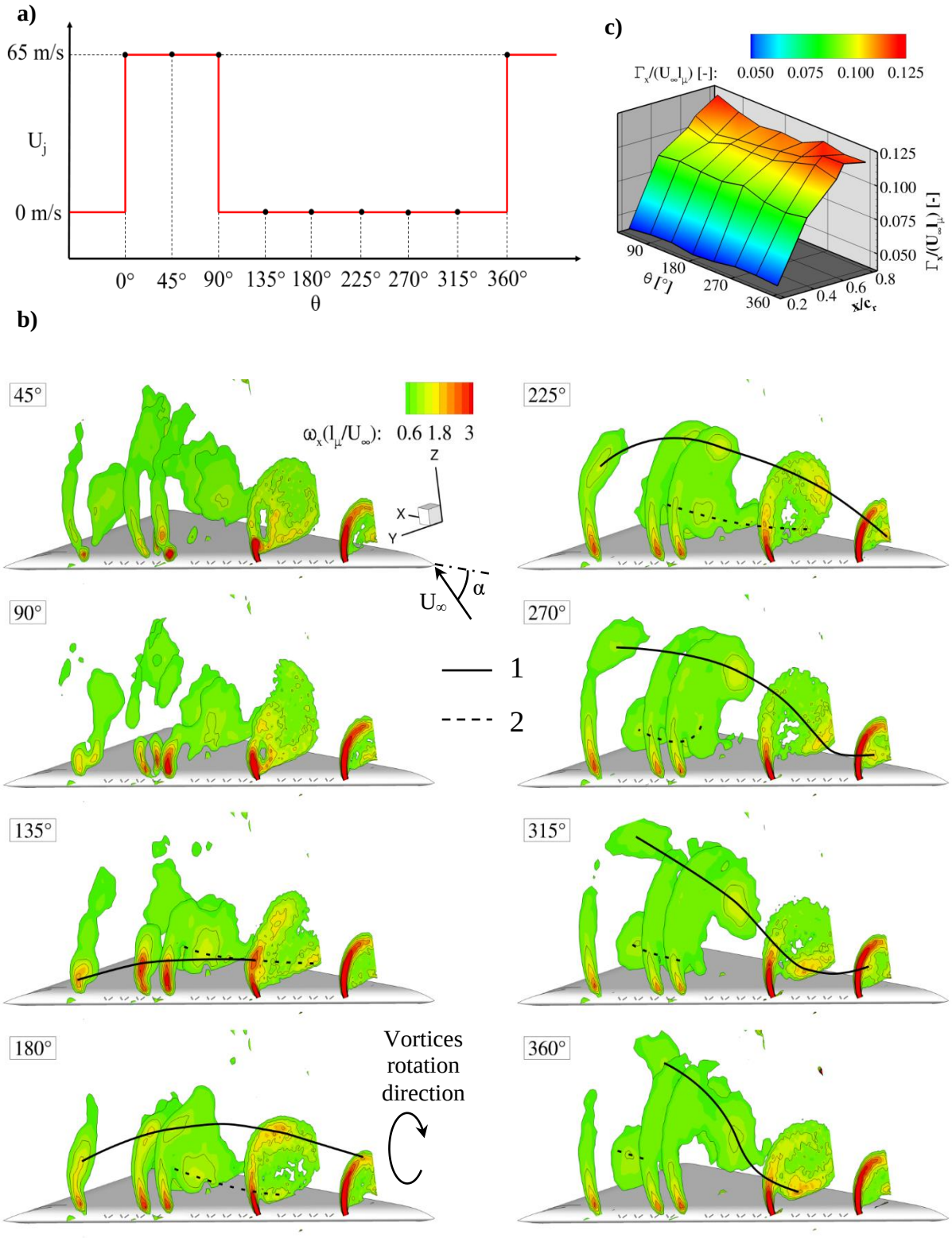

Fig. 10. a) Jet velocity U_j as a function of the phase angle θ during one blowing period.

b) Dimensionless positive axial vorticity $\omega_x/(l_\mu \cdot U_\infty)$ in the cross-flow planes x/c_r = 0.2, 0.4, 0.6, 0.65 and 0.8, at eight phases during one blowing period of F12 (F^+ = 1), at $Re_{l\mu} = 5 \cdot 10^5$, Ma = 0.036 and α = 45°.

c) Dimensionless positive circulation $\Gamma_x/(U_\infty \cdot l_\mu)$ plotted as function of phase angle θ and chord position x/c_r.

A detailed axial vorticity distribution in space and time (or phase) is shown in Fig. 10b. During the first two phases $\theta = 45°, 90°$ the blowing jets produce local vortex pairs. These can be observed in the first two plots at $x/c_r = 0.40$ and $x/c_r = 0.65$. Subsequent to the closing of the valves vortex rotation and downstream convection is observed. By connecting the vorticity peaks with a spline, the axis of the three-dimensional vortices can be reconstructed. From this analysis two large vortices are observed (in Fig. 10b these vortices are distinguished by numbers: vortex "1" and "2"). The vortex 1 is shed from the shear layer at $\theta = 135°$. The second vortex is located further inboard. These vortices do not have straight axis but rather a spiraling one. During the phases in which the valves are closed, the vortices rotate clockwise in stream-wise direction but do not pair up. With time passing these vortical structures are transported downstream and the process is repeated in each period.

5 Summary

Experimental analysis on pulsed LE blowing in the post-stall flight regime of a generic half delta wing was conducted. For this purposes selected data from force measurements and PIV has been presented. During the analysis different actuation strategies were compared: frequency and phase variation along the leading edge. Both the lift coefficient as well as the velocity vector field demonstrated, that synchronized blowing at the leading edge normal to the wing produces the biggest aerodynamic performance enhancement. At the investigated angle of attack of $\alpha = 45°$ a lift increase of 55.1% was achieved. The unsteady momentum through active flow control entrains the separated shear layer and provokes a flow reattachment, responsible for the lift enhancement. Eight sequences of phase-averaged PIV crossflow planes showing the positive axial vorticity field presented the time evolution during one blowing period. The presence of two large vortices was registered, which rotate around the reverse-flow region above the wing and are transported downstream.

Acknowledgement

The authors would like to thank the German Research Association (Deutsche Forschungsgemeinschaft, DFG) for the funding of the project.

References

[1] Gursul J. Review of unsteady vortex flows over slender delta wings. *Journal of Aircraft*, Vol. 42, No. 2, pp 299-319, 2005.

[2] Lucca-Negro O and O'Doherty T. Vortex breakdown: A review. *Progress in Energy and Combustion Science*, Vol. 27, No. 4, pp 431-481, 2001.

[3] Kölzsch A and Breitsamter C. Delta wing flow control for the stall and post-stall regimes. *Deutscher Luft- und Raumfahrt Kongress*, 2014.

[4] Breitsamter C. Unsteady flow phenomena associated with leading-edge vortices. *Progress in Aerospace Sciences.* Vol. 44, No.1, pp 48-56, 2008

[5] Gad-El-Hak M and Blackwelder R F. The discrete vortices from a delta wing. *AIAA Journal*, Vol. 23, No. 6, pp 961-962, 1985

[6] Mitchell A M, Morton S A, Forsythe J R and Cummings R M. Analysis of delta-wing vortical substructures using detached-eddy simulation. AIAA Journal, Vol. 44, No. 5, pp 964-972, 2006

[7] Menke M, Yang H and Gursul I. Experiments on the unsteady nature of vortex breakdown over delta wings. *Experiments in Fluids*. Vol. 27, No. 3, pp 262-272, 1999.

[8] Gursul I, Wang I, and Vardaki E. Review of flow control mechanisms of leading-edge vortices. *Progress in Aerospace Science*, Vol. 43, pp 246−270, 2007.

[9] Mitchell A M, and Delery J. Research into vortex breakdown control. *Progress in Aerospace Sciences*, Vol. 37, pp 385-418, 2001.

[10] Margalit S, Greenblatt D, Seifert A and Wygansky I. Delta wing stall and roll control using segmented piezoelectric fluidic actuators. *Journal of Aircraft*. Vol. 42, No. 3, pp 698-709, 2005.

[11] Gad-el-Hak M, Blackwelder RF. Control of the discrete vortices from a delta wing. *AIAA Journal*. Vol. 25, No. 8, pp 1042-1049. 1987.

[12] Gu W, Robinson O, Rockwell D. Control of vortices on a delta wing by leading-edge injection. *AIAA Journal*. Vol. 31, No. 7, pp 1177-1186, 1993.

[13] Siegel SG, McLaughlin TE, Morrow JA. PIV measurements on a delta wing with periodic blowing and suction. *AIAA 19th Applied Aerodynamics Conference*, Anaheim CA, 2001.

[14] Kölzsch A and Breitsamter C. Vortex-flow manipulation on a generic delta-wing configuration. *Journal of Aircraft*. Vol 51, No. 5, pp 1380-1390, 2014.

[15] Chu J and Luckring JM. Experimental surface pressure data obtained on 65° delta wing across Reynolds number and Mach number ranges. *NASA TM 4645*, 1995.

[16] Hummel D. Review of the second international vortex flow experiment (VFE-2), *46th AIAA Aerospace Sciences Meeting and Exhibit*, AIAA Paper 2008-377, 2008.

[17] Luckring JM and Hummel D. What was learned from the VFE-2 experiments? *46th AIAA Aerospace Sciences Meeting and Exhibit*, AIAA Paper 2008-383, 2008.

[18] Stanislas M, Okamoto K, Kähler CJ and Westerweel J. Main results of the second international PIV challenge, *Experiments in Fluids*, Vol. 39, No. 2, pp 170-191, 2005.

Contact Author Email Address

Mailto: andrei.buzica@tum.de

Copyright Statement